# Ferromagnetism with in-plane magnetization, Dirac spin-gapless semiconducting properties, and tunable topological states in two-dimensional rare-earth metal dinitrides

Yawei Yu, Xin Chen, Xiaobiao Liu, Jia Li, Biplab Sanyal, Xiangru Kong, François M. Peeters, and Linyang Li

Phys. Rev. B **105**, 024407 — Published 6 January 2022

DOI: 10.1103/PhysRevB.105.024407

**Ferromagnetism with in-plane magnetization, Dirac spin-gapless semiconducting property, and tunable topological states in two-dimensional rare-earth-metal dinitrides**

Yawei Yu,[1,*] Xin Chen,[2,*] Xiaobiao Liu,[3] Jia Li,[1] Biplab Sanyal,[2] Xiangru Kong,[4,†] François M. Peeters,[5,6] and Linyang Li[1,‡]

[1]*School of Science, Hebei University of Technology, Tianjin 300401, China*

[2]*Department of Physics and Astronomy, Uppsala University, SE-75120 Uppsala, Sweden*

[3]*School of Science, Henan Agricultural University, Zhengzhou 450002, China*

[4]*Center for Nanophase Materials Sciences, Oak Ridge National Laboratory, Oak Ridge, Tennessee 37831, USA*

[5]*Department of Physics and Astronomy, Key Laboratory of Quantum Information of Yunnan Province, Yunnan University, Kunming 650091, China*

[6]*Department of Physics, University of Antwerp, Groenenborgerlaan 171, B-2020 Antwerp, Belgium*

[*] Yawei Yu and Xin Chen contributed equally to this work.

[†]Corresponding author: kongx@ornl.gov

[‡]Corresponding author: linyang.li@hebut.edu.cn

**ABSTRACT**

Since the successfully synthesis of bulk single-crystals $MoN_2$ and $ReN_2$, which have a layered structure, transition-metal dinitrides have attracted considerable attention in recent years. Here, we focus on rare-earth-metal (Rem) elements, and propose seven stable Rem dinitride monolayers with a 1T structure, namely 1T-$RemN_2$. We use first-principles calculations, and find that these monolayers have a ferromagnetic ground state with in-plane magnetization. Without spin-orbit coupling (SOC), the band structures are spin-polarized with Dirac points at the Fermi level. Remarkably, the 1T-$LuN_2$ monolayer exhibits an isotropic magnetocrystalline anisotropy energy in the *xy*-plane with in-plane magnetization, indicating easy tunability of the magnetization direction. When rotating the magnetization vector in the *xy*-plane, we proposed a model that accurately describes the variation of the SOC band gap and the two possible topological states (Weyl-like semimetal and Chern insulator states), whose properties are tunable. The Weyl-like semimetal state is a critical point between the two Chern insulator states with opposite sign of the Chern numbers (±1). The nontrivial band gap (up to 60.3 meV) and the Weyl-like semimetal state are promising for applications in spintronic devices.

**KEYWORDS:** 2D rare-earth-metal dinitrides, ferromagnetic ground state, in-plane magnetization, Weyl-like semimetal, Chern insulator

## I. Introduction

Comparing to bulk materials, lower dimensional materials have the possibility to generate a multitude of new physical and chemical properties. Since the discovery of graphene [1] and $MoS_2$ [2], we witness a boom in the two-dimensional (2D) material era. Among those 2D materials, transition-metal dinitrides, which exhibit a similar structure as $MoS_2$, have attracted considerable attention in recent years. Bulk single-crystals $MoN_2$ and $ReN_2$ have a layered structure and can be successfully synthesized experimentally [3,4]. Since the van der Waals interactions between the layers are very weak, $ReN_2$ films have been realized by exfoliating from its bulk material [4]. The $MoN_2$ monolayer was theoretically predicted, where ferromagnetic (FM) and antiferromagnetic (AFM) states correspond to two structural phases [5,6]. In this monolayer, the N-N bond is very important for this magnetic phase transition. Using high-throughput calculations, Liu *et al.* proposed a series of monolayers of transition-metal dinitride, such as 1T-$NbN_2$ and 1T-$TaN_2$, which are ferromagnetic [7]. Due to the experimental feasibility and rich magnetic properties of these monolayers, it is thus an interesting question to search for more classes of stable monolayers of transition-metal dinitride.

In 2D FM materials, the appearance of Dirac spin-gapless semiconductors (DSGSs) is very important for spintronics due to the fully spin-polarized band structure and the Dirac points at the Fermi level [8-12]. Generally speaking, when including the spin-orbit coupling (SOC) effect, the Dirac point can be turned into a band gap, and the DSGS can becomes a Chern insulator. The latter has attracted extensive interests due to the realization of the quantum anomalous Hall (QAH) effect [13,14]. Notice that studies of Chern/QAH insulators often assume that the magnetization direction is perpendicular to the plane (out-of-plane) of the 2D system, neglecting the in-plane magnetization [15]. The out-of-plane/in-plane magnetization is determined by the magnetocrystalline anisotropy energy (MAE). Although 2D FM materials with perpendicular magnetocrystalline anisotropy have been the subject of numerous studies due

to their applications in high-density magnetic recording and spintronic devices [16,17], monolayers with in-plane magnetization have the advantage of tunability of the magnetization direction [18], leading to changes in the band structure, which is called the magneto band-structure effect [19]. This is one of the main motivations to study 2D FM materials with in-plane magnetization.

In this work, we focus on a special class kind of transition-metal elements, rare-earth-metal (Rem) elements (Sc, Y, and Lanthanides), and propose new Rem dinitride single layers with a 1T crystal structure, namely 1T-Rem$N_2$. Since 1T-Y$N_2$ [20,21], 1T-La$N_2$ [22], and 1T-Gd$N_2$ [23] have been investigated in detail, we focus on the other Rem elements. Here, we investigate seven Rem elements (Tb-Lu), and propose the corresponding 1T-Rem$N_2$ monolayers, including 1T-Tb$N_2$, 1T-Dy$N_2$, 1T-Ho$N_2$, 1T-Er$N_2$, 1T-Tm$N_2$, 1T-Yb$N_2$, and 1T-Lu$N_2$. By employing first-principles calculations, the structure, dynamical stability, magnetic property, and band structure without SOC of these monolayers were investigated. Then we used the 1T-Lu$N_2$ monolayer as a typical example to investigate the MAE, band structure with SOC, and its tunable topological states.

## II. Computational method

First-principles calculations were performed using the Vienna *ab initio* simulation package (VASP) code [24-26], implementing density functional theory (DFT). For the electron exchange-correlation functional, we used the generalized gradient approximation (GGA) in the form proposed by Perdew, Burke, and Ernzerhof (PBE) [27]. The atomic positions and lattice vectors were fully optimized using the conjugate gradient (CG) scheme until the maximum force on each atom was less than 0.01 eV/Å. The energy cutoff of the plane-wave basis was set to 520 eV with an energy precision of $10^{-6}$ eV in structural optimization, and a higher energy precision of $10^{-8}$ eV was used in other calculations. The Brillouin zone (BZ) was sampled by using a 27×27×1 Γ-centered Monkhorst-Pack grid. The vacuum space was set to at

least 20 Å in all the calculations to minimize artificial interactions between neighboring slabs. The phonon spectrum was calculated using the PHONOPY code [28].

## III. Structure and stability

Fig. 1(a) shows the optimized crystal structure of 1T-$LuN_2$ monolayer. One Lu atom is bonded with six N atoms to form a stable hexagonal lattice and the space/point group is $P$-3$m$1/$D_{3d}$. As a common structural phase [29], the 1T structure has been widely studied theoretically [7,30] and experimentally [31-33]. The optimized lattice constant, Lu-N bond length, and N-N distance along the $z$-axis are 3.64, 2.28, and 1.77 Å, respectively. The dynamical stability of the 1T-$LuN_2$ monolayer is confirmed by its phonon spectrum. As illustrated in Fig. 1(b), no imaginary phonon modes are present, confirming the structural dynamical stability of 1T-$LuN_2$ monolayer. Besides the 1T phase, the 1H phase is also important for 2D materials. The 1H-$LuN_2$ monolayer also shows a phonon spectrum without imaginary phonon modes and its total energy is lower than that of 1T-$LuN_2$ monolayer. The stable 1T and 1H structural phases indicate the flexibility of Lu-N bonds and experimental feasibility of different 2D $LuN_2$ compounds, which is similar to the $VSe_2$ monolayer. Theoretically, both $VSe_2$ monolayers (1T and 1H) exhibit a stable phonon spectrum without imaginary phonon modes [34]. Experimentally, the 1T-$VSe_2$ monolayer has been achieved [35], and a phase transformation from T-phase to H-phase can take place in infrared radiated $VSe_2$ samples [36].

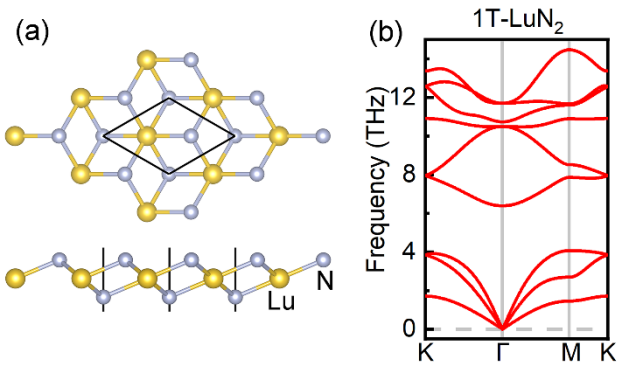


**FIG. 1.** (a) The optimized crystal structure with top and side views of 1T-$LuN_2$ monolayer. (b) The corresponding phonon spectrum along the high-symmetry path of the first BZ.

The optimized structural parameters for the other six 1T-$RemN_2$ monolayers are summarized in Table I. The bond length of Rem-N exhibits the phenomenon of lanthanide shrinkage, where the atomic radius decreases with increasing atomic number. The cohesive energy can be obtained from the equation $E_{coh} = (E_{RemN2} - E_{Rem} - 2E_N)/3$, where $E_{RemN2}$, $E_{Rem}$, and $E_N$ are the total energy of 1T-$RemN_2$ monolayer (per unit cell), of a single Rem atom, and of a single N atom, respectively [22]. The calculated cohesive energy is between −4.33 eV/atom and −4.28 eV/atom, proving the experimental feasibility of 1T-$RemN_2$ monolayers and the chemical similarity of the Rem elements. Additionally, in order to confirm the dynamical stability of the other six 1T-$RemN_2$ monolayers, the phonon spectra are shown in Fig. S1 (Part I of Supplemental Material) [37]. There are no imaginary frequency modes, indicating their dynamical stability. The phonon spectra of the seven 1T-$RemN_2$ monolayers are similar with a low cutoff frequency of acoustic phonons, indicating that these structures are expected to show a low lattice thermal conductivity [22,38,39]. This property makes 1T-$RemN_2$ monolayers promising as thermoelectric materials.

**TABLE I.** Optimized structural parameters of the 1T-$RemN_2$ monolayers. The $a$, $l$, and $h$ are the lattice

constant, bond length of Rem-N, and N-N distance along the *z*-axis, respectively. The unit of the cohesive energy $E_{coh}$ is eV/atom.

| 1T-Rem$N_2$ | *a* (Å) | *l* (Å) | *h* (Å) | $E_{coh}$ |
|---|---|---|---|---|
| 1T-Tb$N_2$ | 3.78 | 2.36 | 1.77 | −4.31 |
| 1T-Dy$N_2$ | 3.75 | 2.34 | 1.77 | −4.29 |
| 1T-Ho$N_2$ | 3.73 | 2.33 | 1.77 | −4.32 |
| 1T-Er$N_2$ | 3.71 | 2.32 | 1.77 | −4.28 |
| 1T-Tm$N_2$ | 3.69 | 2.30 | 1.77 | −4.33 |
| 1T-Yb$N_2$ | 3.66 | 2.29 | 1.77 | −4.32 |
| 1T-Lu$N_2$ | 3.64 | 2.28 | 1.77 | −4.32 |

**IV. Magnetic property**

To investigate the magnetic ground state, five initial magnetic configurations in a 2×2 supercell were considered, including ferromagnetic (FM), Néel antiferromagnetic (NAFM), stripy antiferromagnetic (SAFM), zigzag antiferromagnetic (ZAFM), and nonmagnetic (NM) states [15]. For 1T-Lu$N_2$ monolayer, the spin-polarized electron density of the FM/NAFM/SAFM/ZAFM state is shown in Fig. S2 (Part II of Supplemental Material) [37]. The total energy of the NAFM/SAFM/ZAFM/NM state is 295/209/196/390 meV per unit cell relative to that of the FM state, which indicates that the magnetic ground state is FM for 1T-Lu$N_2$ monolayer. The 2×2 supercell with the FM state exhibits 12 $\mu_B$ magnetic moment (3 $\mu_B$ per unit cell), and most of the magnetic moment is contributed by the N atoms, as shown in Fig. S2(a). By comparing the total energy of the FM and AFM (NAFM/SAFM/ZAFM) states with magnetic moment of $M \approx 1.5\mu_B$ per N atom, the three exchange parameters $J_1 = 8.6$ meV, $J_2 = 1.5$ meV, and $J_3 = 2.4$ meV

can be obtained, which correspond to the first, second and third nearest-neighbor magnetic exchange interactions, respectively [20]. Using the mean-field theory (MFT) [40], the Curie temperature ($T_c$) can be estimated, and the details are shown in Part II of Supplemental Material [37]. The calculated results of total energy for the FM/NAFM/SAFM/ZAFM/NM state of the other six 1T-Rem$N_2$ monolayers are summarized in Table II, which indicates that the magnetic ground state is FM (magnetic moment of 3 $\mu_B$ per unit cell) for all the 1T-Rem$N_2$ monolayers.

**TABLE II.** Total energy (meV per unit cell) of the different magnetic state with respect to *E*(FM). The unit of MAE determined by the equation $E(001) - E(100)$ and the two fitting coefficients $K_1$ and $K_2$ is μeV per unit cell.

| 1T-Rem$N_2$ | *E*(NAFM) | *E*(SAFM) | *E*(ZAFM) | *E*(NM) | MAE | $K_1$ | $K_2$ |
|---|---|---|---|---|---|---|---|
| 1T-Tb$N_2$ | 409 | 273 | 292 | 513 | 460 | 400.0 | 59.67 |
| 1T-Dy$N_2$ | 389 | 262 | 275 | 493 | 536 | 481.2 | 54.34 |
| 1T-Ho$N_2$ | 368 | 250 | 259 | 472 | 602 | 551.8 | 50.47 |
| 1T-Er$N_2$ | 350 | 240 | 243 | 453 | 669 | 619.9 | 48.86 |
| 1T-Tm$N_2$ | 331 | 229 | 227 | 431 | 707 | 662.0 | 45.16 |
| 1T-Yb$N_2$ | 310 | 217 | 209 | 407 | 907 | 842.4 | 64.15 |
| 1T-Lu$N_2$ | 295 | 209 | 196 | 390 | 860 | 811.6 | 48.60 |

We further calculated the MAE of the FM ground state. The MAE is defined as the required energy to rotate the magnetization direction from the easy axis to the hard axis [41], which can be described as MAE = *E*(hard axis) − *E*(easy axis) [16]. It is widely accepted that the MAE correlates with the thermal

stability of magnetic data storage. Generally, the larger the MAE, the more stable the magnetization and thus the better the performance for data storage [42]. To calculate the MAE of the FM ground state, we included the SOC and calculated total the energy of 1T-$LuN_2$ monolayer with magnetization vector $\hat{\boldsymbol{m}}$ constrained in different directions in the *zx*-plane, *zy*-plane, and *xy*-plane. The azimuth angle $\theta$ in the *zx*-plane/*zy*-plane is the angle between the magnetization vector $\hat{\boldsymbol{m}}$ and the positive direction of *z*-axis (001-direction) while the horizontal azimuth angle $\varphi$ in the *xy*-plane is the angle between the magnetization vector $\hat{\boldsymbol{m}}$ and the positive direction of *x*-axis (100-direction). The MAE in the *zx*-plane/*zy*-plane is calculated from the equation $\mathrm{MAE}(\theta) = E(001) - E(\theta)$ while the MAE in the *xy*-plane is obtained as $\mathrm{MAE}(\varphi) = E(001) - E(\varphi)$. The MAE as a function of $\theta / \varphi$ ranging from 0° to 360° is shown in Fig. 2, and $\mathrm{MAE} \geq 0$ can be found. In Fig. 2(a) and (b), the angle of $\theta = 0° / 180°$ corresponds to the smallest MAE while the angle of $\theta = 90° / 270°$ corresponds to the largest MAE, proving the *x*-axis/*y*-axis should be the easy axis. For the *xy*-plane (Fig. 2(c)), the energy difference between maximum and minimum is less than 0.5 μeV per unit cell, implying essential isotropy and therefore it is an easy plane (*xy*-plane). Hence, 1T-$LuN_2$ monolayer has in-plane magnetization with isotropic MAE in the *xy*-plane, similar as found previously for $VS_2$ monolayer [43].

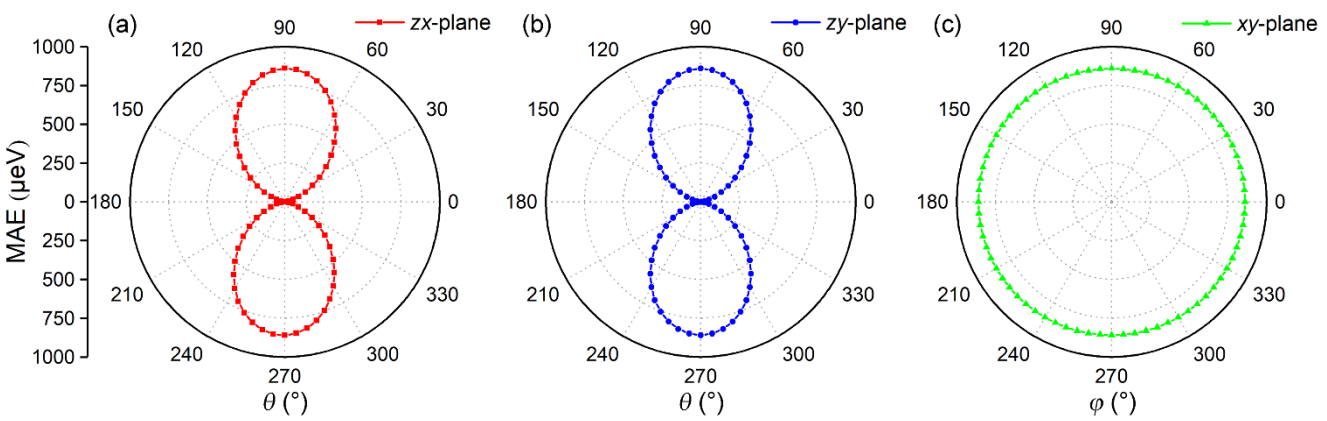


**FIG. 2.** MAE (1T-$LuN_2$) as a function of the azimuthal angle $\theta$ between the magnetization direction $\hat{\boldsymbol{m}}$

and the positive direction of *z*-axis (001-direction) in the *zx*-plane (a) and *zy*-plane (b). MAE (1T-$LuN_2$) as a function of the azimuthal angle $\varphi$ between the magnetization direction $\hat{\boldsymbol{m}}$ and the positive direction of *x*-axis (100-direction) in the *xy*-plane (c).

However, not all FM monolayers with in-plane magnetization exhibit isotropic MAE in the *xy*-plane. For the theoretical $OsCl_3$ and $PtCl_3$ monolayers, it was found that the total energy for the different magnetization directions in the *xy*-plane can be anisotropic [15,18]. Since the 1T-$LuN_2$ monolayer exhibit isotropic MAE in the *xy*-plane, the MAE of our hexagonal crystal can be fitted as $\mathrm{MAE}(\theta) = K_1 \sin^2\theta + K_2 \sin^4\theta$ [23,44]. Based on our DFT results of *zx*-plane (bule squares in Fig. 3(h)), we obtain the two fitting coefficients, $K_1$ = 811.6 μeV per unit cell and $K_2$ = 48.60 μeV per unit cell. The fitting curve (red curve in Fig. 3(h)) agrees well with our DFT results (bule squares in Fig. 3(h)), and the maximum value of MAE corresponding to $\theta = 90°$ (100-direction) is 860 μeV per unit cell, indicating its considerable stability of the in-plane magnetization. For the 1T-$TbN_2$/1T-$DyN_2$/1T-$HoN_2$/1T-$ErN_2$/1T-$TmN_2$/1T-$YbN_2$ monolayer, the MAE of DFT results (blue squares) and fitting curve (red curve) as a function of $\theta$ (*zx*-plane) are shown in Fig. 3(b)/(c)/(d)/(e)/(f)/(g). Similar to the results of 1T-$LuN_2$ monolayer in Fig. 3(h), all of them exhibit a hard axis along the *z*-axis ($\theta = 0°/180°$) while the easy axis is along 100-direction ($\theta = 90°$). For each 1T-$RemN_2$ monolayer, the maximum value of MAE ($\theta = 90°$, 100-direction) and the fitting coefficients ($K_1$ and $K_2$) are summarized in Table II. It can be concluded that all the seven 1T-$RemN_2$ monolayers exhibit in-plane magnetization. After averaging the maximum values of MAE per magnetic atom (230~453.5 μeV per N atom), these values are comparable to the MAE value of $VS_2$ (≈ 300 μeV per V atom)/ VOOH monolayer (294 μeV per V atom) [43,45], which also exhibits in-plane magnetization. MAE is of vital importance in stabilizing the 2D ferromagnetism. Although the magnetic state in these monolayers can be modelled by a XY model [46], which exhibits a quasi-long-

range FM ordering in a finite temperature range [43,45], the recent achievement of in-plane magnetization in a 1T-$VSe_2$ monolayer indicates that such a limitation can be overcome in experiment [35]. However, for another Rem element, La [22], the situation is opposite by using the same equation $\mathrm{MAE}(\theta) = E(001) - E(\theta)$. In Fig. 3(a), $\mathrm{MAE} \leq 0$ represents out-of-plane magnetization for 1T-$LaN_2$ monolayer (the easy axis is along *z*-axis), which is similar to the two experimental FM monolayers, $CrI_3$ [47] and $Fe_3GeTe_2$ [48]. For the above three experimentally obtainable monolayers, including 1T-$VSe_2$ [34,49], $CrI_3$ [50,51], and $Fe_3GeTe_2$ [52], the SOC induced MAE from calculations are 1200/183, 339/349, and 520/920 (μeV per magnetic atom), respectively. Since the MAE values for the seven 1T-$RemN_2$ monolayers are the same magnitude as these experimental monolayers, we conclude that ferromagnetism with in-plane magnetization will be preferable and stabilized spontaneously.

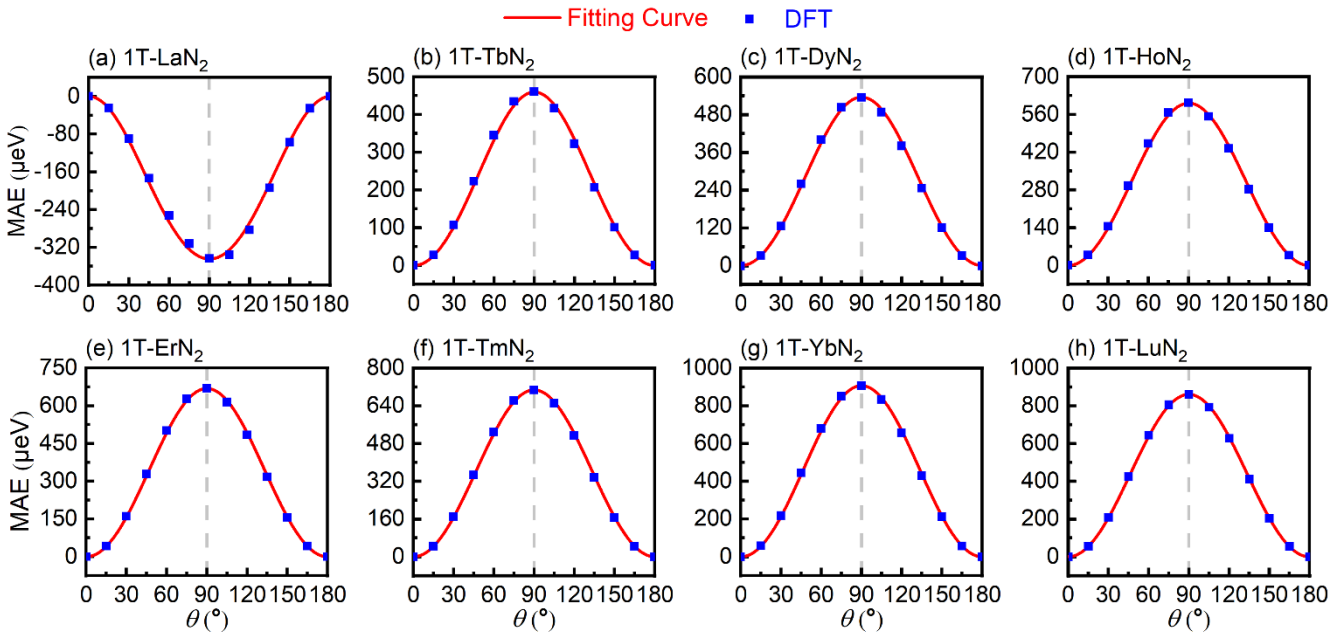


**FIG. 3.** MAE as a function of azimuth angle $\theta$ in the *zx*-plane for 1T-$LaN_2$ (a)/1T-$TbN_2$ (b)/1T-$DyN_2$ (c)/1T-$HoN_2$ (d)/1T-$ErN_2$ (e)/1T-$TmN_2$ (f)/1T-$YbN_2$ (g)/1T-$LuN_2$ (h) monolayer. The blue squares are from DFT calculations and the red curves are the fitting curves.

**V. Band structure and topological state**

Next, the electronic band structures of the seven 1T-Rem$N_2$ monolayers were calculated. In Fig. 4 (b), the spin-polarized band structure without SOC of 1T-Lu$N_2$ monolayer is shown. The blue/red bands correspond to the majority-spin/minority-spin (spin-up/spin-down) channels [53], and a giant spin-splitting can be observed. In the majority-spin bands, there is a semiconducting band gap between the valence and conduction bands around the Fermi level. In the minority-spin bands, there is a linear Dirac point (insert of Fig. 4(b)) at the D point of the first BZ, which is the intersection of the valence and conduction bands at the Fermi level. Since the majority-spin electrons are semiconducting while the minority-spin electrons are metallic (semimetallic), broadly speaking, the 1T-Lu$N_2$ monolayer should exhibit a half-metallic behavior [54]. For the hexagon of the first BZ, D is along the high-symmetry path M-K, and there are twelve Dirac points, as shown in Fig. 4(a) and (c). To further understand the formation of the Dirac point, the projected band structures of 1T-Lu$N_2$ monolayer for the different atoms and different atomic orbitals (without SOC) are shown in Fig. S3 (Part III of Supplemental Material) [37]. At first, the contributions of the different atoms should be distinguished. The (a) and (b) of Fig. S3 illustrate that the energetic states near the Fermi level are mainly contributed by the nitrogen atoms, while the contributions of the Lutetium atoms are very small. Furthermore, the different atomic orbital contributions of the nitrogen atoms are shown in (c), (d), (e) and (f) of Fig. S3. The energetic states near the Fermi level including the Dirac point are mainly contributed by the *p* ($p_x$, $p_y$ and $p_z$) atomic orbital, rather than the *s* atomic orbital. In other words, the 1T-Lu$N_2$ monolayer should be a Dirac spin-gapless semiconductor (DSGS) of *p*-state [9-12,22]. The other six 1T-Rem$N_2$ monolayers exhibit a similar band structure of DSGS, as shown in Fig. 4(d)-(i). The above results of band structure without SOC are in good agreement with previous reports on 1T-Rem$N_2$ monolayer [20-23].

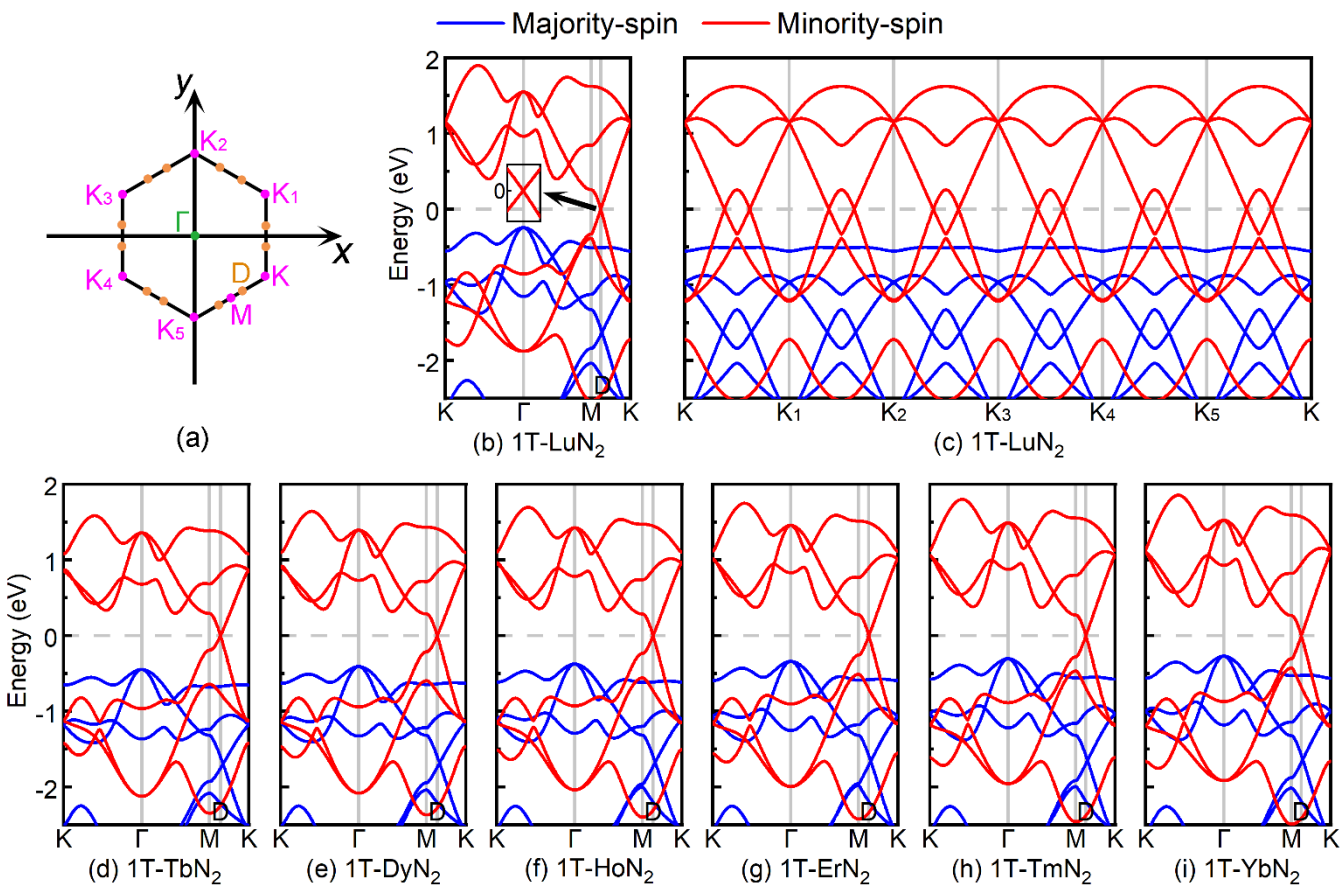


**FIG. 4.** (a) Hexagon of the first BZ and positions of the Dirac point indicated by orange dots. (b)/(c) Band structure without SOC of the 1T-$LuN_2$ monolayer. (d)-(i) Band structures without SOC of the other six 1T-$RemN_2$ monolayers.

For the FM monolayers with out-of-plane magnetization, such as $CrI_3$ [47], $Fe_3GeTe_2$ [48], and $FeB_3$ [55], the easy axis is along the *z*-axis, leading to the uniqueness of the band structure with SOC from the view of lowest total energy. In view of the MAE for 1T-$LuN_2$ monolayer, each direction in the *xy*-plane should be the easy magnetization direction due to the isotropic MAE in the *xy*-plane. Hence, we need to investigate the band structure with SOC along each direction in the *xy*-plane. When SOC is not included, the Dirac point is located along the high-symmetry path M-K, and there are twelve Dirac points in the hexagon of the first BZ, as shown in Fig. 4(a) and (c). We considered the SOC effect for this Dirac band structure of 1T-$LuN_2$ monolayer, and a further study on topological properies was performed by using

WannierTools package [56]. Near the Fermi level, the electronic bands are mainly from $p_x$, $p_y$, and $p_z$ atomic orbitals of the N atoms (Fig. S3, Part III of Supplemental Material) [37]. Thus, we constructed an effective tight-binding Hamiltonian with the these $p$ atomic orbitals [57,58]. By the concept of effective principle layers, an iterative procedure to compute the Green's function for a semi-infinite system was performed [59], from which the edge states can be obtained.

We first considered the case of $\varphi = 0°$. The blue arrow in Fig. 5(a) is the direction of magnetization vector $\hat{\boldsymbol{m}}$, which is $\varphi = 0°$ with respect to the positive direction of $x$-axis. When SOC is included, a band gap is opened at each Dirac point (Fig. 5(b)). The global band gaps (between the two red lines) in the path $K_1$-$K_2$/$K_2$-$K_3$/$K_4$-$K_5$/$K_5$-K are 60.3 meV, corresponding to the angle $\alpha = 30°$ between $\hat{\boldsymbol{m}}$ and $K_1K_2$/$K_2K_3$/$K_4K_5$/$K_5$K. The band gaps between the two blue lines in the path K-$K_1$/$K_3$-$K_4$ are 121.7 meV, corresponding to the angle $\alpha = 90°$ between $\hat{\boldsymbol{m}}$ and K$K_1$/$K_3K_4$. Here, we should notice $60.3 \approx 121.7 \times \sin 30°$ and $121.7 = 121.7 \times \sin 90°$. The calculated chiral edge states for $\varphi = 0°$ are shown in Fig. 5(c), and three edge states can be seen. However, only one edge state around the X|X' connects the valence and conduction band areas, confirming that the global band gap of 60.3 meV is nontrivial. This large nontrivial band gap makes it possible to achieve the QAH effect at room temperature. On the other hand, according to the bulk-edge correspondence, one chiral edge state corresponds to the Chern number of $C = +1$, which can be further confirmed by Wannier charge centers (WCCs) and anomalous Hall conductivity (AHC) (Fig. S4(a) and (b), Part IV of Supplemental Material) [37]. For the case of $\varphi = 30°$ (Fig. 5(d) and (e)), $\hat{\boldsymbol{m}}$ is parallel to $K_2K_3$/$K_5$K ($\alpha = 0°$), and the global band gaps in the path $K_2$-$K_3$/$K_5$-K vanish ($0 = 121.7 \times \sin 0°$), leading to four gapless points at the Fermi level. Since each gapless point formed by two linear band lines is robust against SOC and twofold degenerate [18,60,61], these points can be recognized as Weyl-like points (Part V of Supplemental Material) [37,62-66]. The band gaps between the two blue lines in the path K-$K_1$/$K_1$-$K_2$/$K_3$-$K_4$/$K_4$-$K_5$ are 105.1 meV, corresponding to the angle $\alpha = 60°$ between $\hat{\boldsymbol{m}}$

and $KK_1/K_1K_2/K_3K_4/K_4K_5$ ($105.1 \approx 121.7 \times \sin 60°$). Correspondingly, the obtained edge states are shown in Fig. 5(f), and we observe a clear "Fermi arc" connecting the pair of gapless points. Since the main bands around the Fermi level are not contributed by the *f* atomic orbitals of Lu atom, these gapless points are robust against the Hubbard *U* correction, which is used for describing strong correlated *f* electrons. When the effective value of *U* is equal to 6 eV according to previous work on Rem elements [67,68], these gapless points are kept at the Fermi level, as shown in Fig. S5 (Part V of Supplemental Material) [37]. However, the $PtCl_3$ monolayer can be transformed into a Mott insulator when $U > 2.8$ eV [18]. For the case of $\varphi = 60°$ (Fig. 5(g) and (h)), the values of the band gaps are similar to the one for $\varphi = 0°$. The global band gaps (between the two red lines) in the path $K\text{-}K_1/K_2\text{-}K_3/K_3\text{-}K_4/K_5\text{-}K$ are 60.3 meV, corresponding to the angle $\alpha = 30°$ between $\hat{\boldsymbol{m}}$ and $KK_1/K_2K_3/K_3K_4/K_5K$ ($60.3 \approx 121.7 \times \sin 30°$). The band gaps between the two blue lines in the path $K_1\text{-}K_2/K_4\text{-}K_5$ are 121.7 meV, corresponding to the angle $\alpha = 90°$ between $\hat{\boldsymbol{m}}$ and $K_1K_2/K_4K_5$ ($121.7 = 121.7 \times \sin 90°$). Correspondingly, the obtained edge states are shown in Fig. 5(i). One edge state connects the valence and conduction band areas, illustrating that the band gap of 60.3 meV is also nontrivial. However, comparing the edge states of $\varphi = 0°$ (Fig. 5(c)), it is counter propagating for the case of $\varphi = 60°$, which indicates that the Chern number has opposite sign ($C = -1$), which can be further confirmed by WCCs and AHC (Fig. S4(d) and (e), Part IV of Supplemental Material) [37].

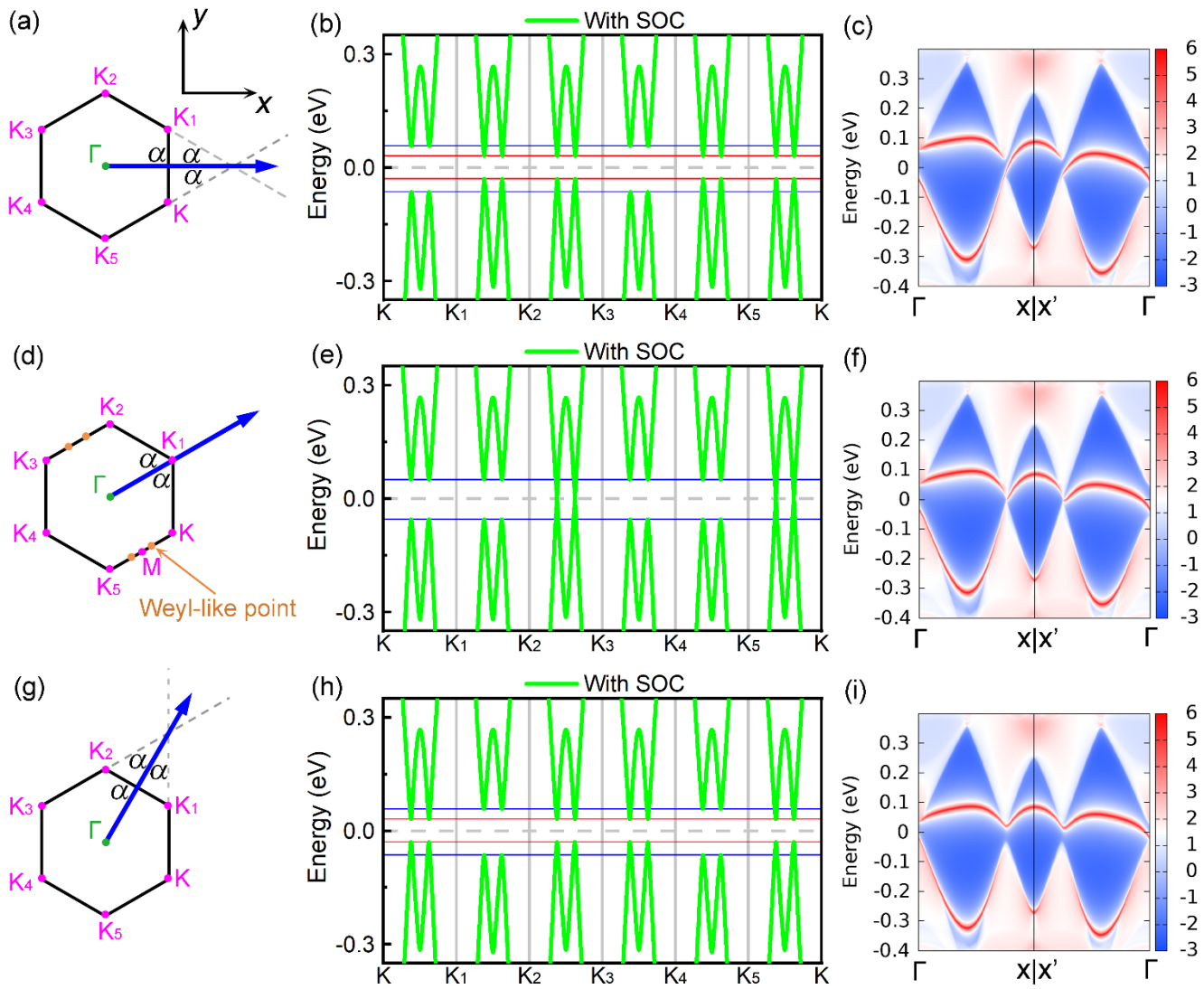


**FIG. 5.** The direction of magnetization vector $\hat{\boldsymbol{m}}$ (blue arrow) with respect to the positive direction of $x$-axis with angle $\varphi = 0°$ (a), $\varphi = 30°$ (d), and $\varphi = 60°$ (g). The band structure with SOC along the high-symmetry path of K-$K_1$-$K_2$-$K_3$-$K_4$-$K_5$-K (b)/(e)/(h) and the edge states (c)/(f)/(i) for 1T-$LuN_2$ monolayer. (b)(c), (e)(f), and (h)(i) correspond to $\varphi = 0°$ (a), $\varphi = 30°$ (d), and $\varphi = 60°$ (g), respectively.

In the above calculations of the Chern numbers, WCCs are defined as

$$\bar{x}_n(k_y) = \frac{i}{2\pi}\int_{-\pi}^{\pi} dk_x \left\langle u_n(k_x,k_y)\middle|\partial_{k_x}\middle|u_n(k_x,k_y)\right\rangle,$$

where $\left|u_n(k_x,k_y)\right\rangle$ is the periodic part of Bloch function [69]. By tracking the evolution of the sum of hybrid WCCs, Chern number of $C = +1$ can be observed by the upward shift of WCCs (Fig. S4(a), Part

IV of Supplemental Material) [37] in the case of $\varphi = 0°$, while Chern number of $C = -1$ can be observed by the downward shift of WCCs (Fig. S4(d)) in the case of $\varphi = 60°$. Moreover, AHC was also calculated according to

$$\sigma_{xy} = \frac{e^2}{(2\pi)^2 h} \int_{BZ} dk_x dk_y f_n(k_x, k_y) \Omega_{n,z}(k_x, k_y),$$

where $f_n(k_x, k_y)$ is Fermi-Dirac distribution function, and $\Omega_{n,z}(k_x, k_y)$ is Berry curvature [70]. As shown in Fig. S4(b)/(e), there is a plateau of AHC in the nontrivial SOC band gap of bulk state, which satisfies $\sigma_{xy} = Ce^2 / h$, further confirming the Chern number of $C = +1/C = -1$. In order to further understand the topological phase transitions, Berry curvatures are demonstrated in the reciprocal space in Fig. S4(c) and (f). As discussed for 1T-$YN_2$ monolayer (out-of-plane magnetization along 001 direction) [21], the total three pairs of Berry curvature peaks with the same positive sign in the whole BZ contribute the Chern number of $C = +3$. In the case of 1T-$LuN_2$ monolayer (in-plane magnetization with $\varphi = 0°$), one pair of Berry curvature peaks flips its sign to be negative as shown in Fig. S4(c), leading to $C = +1$. In the case of $\varphi = 60°$, two pairs of Berry curvature peaks flip its sign to be negative as shown in Fig. S4(f), leading to $C = -1$.

Essentially, $\alpha (0° \le \alpha \le 90°)$ is the angle between $\hat{\boldsymbol{m}}$ and the $C_2$ symmetry axis. Due to the $C_{3z}$ symmetry, there are three $C_2$ symmetry axes, $C_{2y}$ (□ $KK_1/K_3K_4$), $C_{2+}$ (□ $K_1K_2/K_4K_5$), and $C_{2-}$ (□ $K_2K_3/K_5K$), as shown in Fig. 6(a). When $\hat{\boldsymbol{m}}$ is parallel to the $C_{2-}/C_{2y}/C_{2+}$ axis, the $C_2$ symmetry can be protected, leading to two pairs of Weyl-like points in the corresponding parallel high-symmetry paths [71-76]. When there is an angle $\alpha$ between $\hat{\boldsymbol{m}}$ and the $C_{2-}/C_{2y}/C_{2+}$ symmetry axis, the $C_2$ symmetry can be broken, leading to the absence of Weyl-like points with the opening of a band gap in the corresponding parallel high-symmetry paths. The value of the band gap ($G$) depends on the degree of the broken $C_2$ symmetry, and it can be accurately described by $G = 2\mathrm{g} \times \sin\alpha$, where 2g is equal to 121.7 meV,

corresponding to the value of the maximum SOC band gap in the high-symmetry path K-$K_1$/$K_3$-$K_4$ ($\alpha = 90°$) in the case of $\varphi = 0°$, and g is also equal to the value of the global SOC band gap in the case of $\varphi = 0°$. Using this model, the value of the SOC band gap on each high-symmetry path (K-$K_1$/$K_1$-$K_2$/$K_2$-$K_3$/$K_3$-$K_4$/$K_4$-$K_5$/$K_5$-K) can be calculated, and then the global SOC band gap can be obtained for each angle of $\varphi$ in the *xy*-plane, as shown in Fig. 6(b) (red curves). To confirm the rationality of this model, we calculated the global SOC band gaps by DFT, as shown in Fig. 6(b) (blue dots). Notice that the two results agree very well, indicating the accuracy of our proposed model.

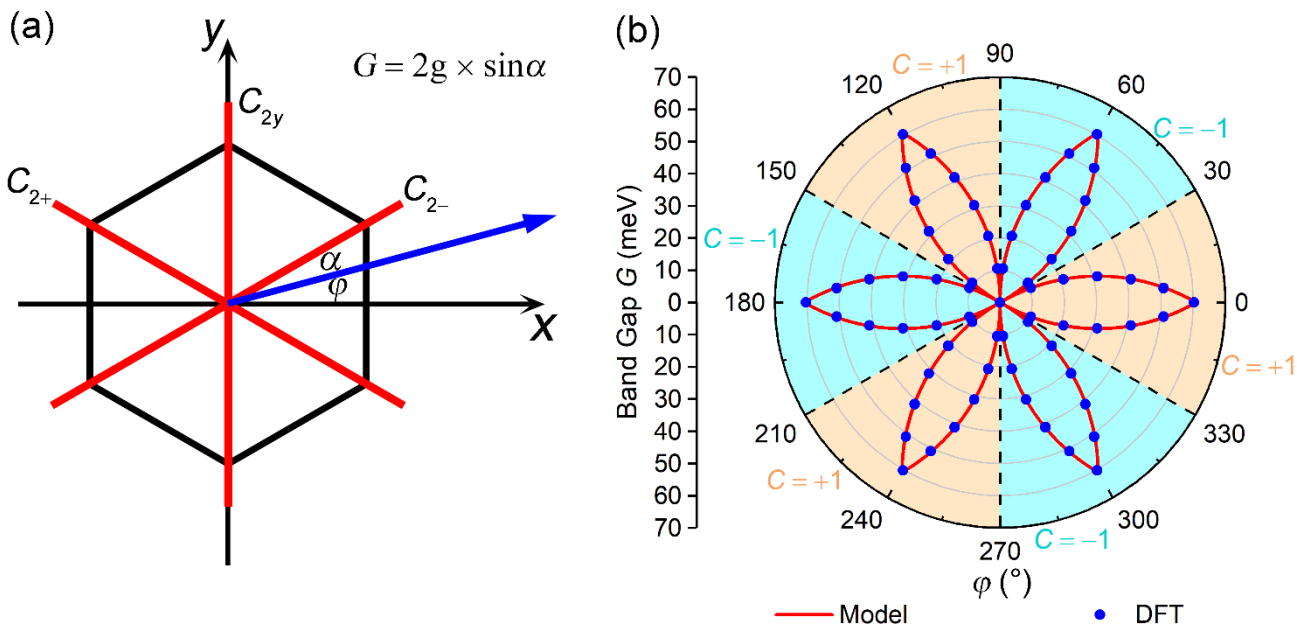


**FIG. 6.** (a) $\alpha$ is the angle between magnetization vector $\hat{\boldsymbol{m}}$ (blue arrow) and the $C_2$ symmetry axis. $\varphi$ is the angle between magnetization vector $\hat{\boldsymbol{m}}$ and the positive direction of *x*-axis. (b) Global SOC band gap of the 1T-$LuN_2$ monolayer as a function of the azimuthal angle $\varphi$ (*xy*-plane) based on the proposed model (red curves) and DFT calculations (blue dots). The different color areas correspond to different Chern numbers ($C = \pm 1$), and the black dashed lines between the different color areas represent the Weyl-like semimetal states (gapless points).

Thus, we have proven that the Weyl-like semimetal state is a critical point between two Chern insulator states with opposite sign of Chern numbers ($C = \pm 1$), leading to tunable topological states when rotating the magnetization vector in the *xy*-plane. By breaking time reversal symmetry and protecting mirror (glide mirror) symmetry, the gapless points under SOC can be realized in other monolayers [18,65,77-83]. In our 1T-$LuN_2$ monolayer, where time reversal symmetry is broken and $C_2$ symmetry is protected, the 2D Weyl-like points can be realized in special magnetization directions of *xy*-plane ( $\varphi = 30° / 90° / 150° / 210° / 270° / 330°$ ). Moreover, a tunable Chern number is also important. Experimentally, a well quantized QAH effect with tunable Chern number (up to $C$ = 5) in multilayer structures has been realized [84]. Theoretically, it has been proven that the irradiation of left/right circularly polarized light can tune the Chern number [85]. In the present work, when the magnetization vector is rotated in the *xy*-plane, it can realize a change of sign of the Chern number $C$, corresponding to a change of propagating direction of the edge channel, making 1T-$LuN_2$ monolayer promising for applications in spintronic devices.

## VI. Conclusion

In summary, using DFT calculations we predict a series of stable 2D rare-earth-metal dinitrides, 1T-$RemN_2$ monolayers, which exhibit a FM ground state (magnetic moment of 3 $\mu_B$ per unit cell). Without SOC, all the considered systems show a spin-polarized electronic band structure, and are a Dirac spin-gapless semiconductor. Taking SOC into account, in-plane magnetization occurs in all the 1T-$RemN_2$ monolayers with a maximum MAE in the range 460~907 μeV per unit cell, indicating the considerable stability of the in-plane magnetization. For the 1T-$LuN_2$ monolayer, the in-plane magnetization exhibits isotropic MAE in the *xy*-plane, indicating easy tunability of the magnetization direction. By rotating the magnetization direction in the *xy*-plane, the value of the nontrivial SOC band gap can be accurately

described by our proposed model. The gapped band structures (up to 60.3 meV) correspond to the Chern insulator state while the gapless band structures correspond to the Weyl-like semimetal state, which is a critical state between two Chern insulator states with opposite sign of the Chern numbers ($C = \pm 1$). The realization of Chern insulator and Weyl-like semimetal states in the 1T-$LuN_2$ monolayer has therefore enriched the family of topological materials.

**Acknowledgements**

This work is supported by the National Natural Science Foundation of China (Grant No. 12004097), the Natural Science Foundation of Hebei Province (Grant No. A2020202031), and the Foundation for the Introduced Overseas Scholars of Hebei Province (Grant No. C20200313). X.L. acknowledges financial support from the National Natural Science Foundation of China (Grant No. 22005087). The computational resources utilized in this research were provided by Shanghai Supercomputer Center. A portion of this work (X.K.) was conducted at the Center for Nanophase Materials Sciences, which is a US Department of Energy Office of Science User Facility. This research used resources of the Compute and Data Environment for Science (CADES) at the Oak Ridge National Laboratory, which is supported by the Office of Science of the U.S. Department of Energy under Contract No. DE-AC05-00OR22725.

**Notes**

The authors declare no competing financial interest.

others to do so, for United States Government purposes. The Department of Energy will provide public access to these results of federally sponsored research in accordance with the DOE Public Access Plan (http://energy.gov/downloads/doe-public-access-plan).

**References**

[1] K. S. Novoselov, A. K. Geim, S. V. Morozov, D. Jiang, Y. Zhang, S. V. Dubonos, I. V. Grigorieva, and A. A. Firsov, Science **306**, 666-669 (2004).

[2] K. S. Novoselov, D. Jiang, F. Schedin, T. J. Booth, V. V. Khotkevich, S. V. Morozov, and A. K. Geim, PNAS **102**, 10451-10453 (2005).

[3] S. Wang, H. Ge, S. Sun, J. Zhang, F. Liu, X. Wen, X. Yu, L. Wang, Y. Zhang, H. Xu, J. C. Neuefeind, Z. Qin, C. Chen, C. Jin, Y. Li, D. He, and Y. Zhao, J. Am. Chem. Soc. **137**, 4815-4822 (2015).

[4] M. Onodera, F. Kawamura, N. T. Cuong, K. Watanabe, R. Moriya, S. Masubuchi, T. Taniguchi, S. Okada, and T. Machida, APL Mater. **7**, 101103 (2019).

[5] Y. Wang, S.-S. Wang, Y. Lu, J. Jiang, and S. A. Yang, Nano Lett. **16**, 4576-4582 (2016).

[6] F. Wu, C. Huang, H. Wu, C. Lee, K. Deng, E. Kan, and P. Jena, Nano Lett. **15**, 8277-8281 (2015).

[7] J. Liu, Z. Liu, T. Song, and X. Cui, J. Mater. Chem. C **5**, 727-732 (2017).

[8] X. L. Wang, Phys. Rev. Lett. **100**, 156404 (2018).

[9] X.-L. Wang, Natl. Sci. Rev., **4**, 252-257 (2017).

[10] X. Wang, T. Li, Z. Cheng, X.-L. Wang, and H. Chen, Appl. Phys. Rev. **5**, 041103 (2018).

[11] Z. Yue, Z. Li, L. Sang, and X. Wang, Small **16**, 1905155 (2020).

[12] X. Wang, Z. Cheng, G. Zhang, H. Yuan, H. Chen, and X.-L. Wang, Phys. Rep. **888**, 1-57 (2020).

[13] C.-Z. Chang, J. Zhang, X. Feng, J. Shen, Z. Zhang, M. Guo, K. Li, Y. Ou, P. Wei, L.-L. Wang, Z.-Q. Ji, Y. Feng, S. Ji, X. Chen, J. Jia, X. Dai, Z. Fang, S.-C. Zhang, K. He, Y. Wang, L. Lu, X.-C. Ma, and

Q.-K. Xue, Science **340**, 167-170 (2013).

[14] Y. Deng, Y. Yu, M. Z. Shi, Z. Guo, Z. Xu, J. Wang, X. H. Chen, and Y. Zhang, Science **367**, 895-900 (2020).

[15] X.-L. Sheng, and B. K. Nikolić, Phys. Rev. B **95**, 201402(R) (2017).

[16] X. Chen, Y. Liu, and B. Sanyal, J. Phys. Chem. C **124**, 4270-4278 (2020).

[17] F. Gimbert, and L. Calmels, Phys. Rev. B **86**, 184407 (2012).

[18] J.-Y. You, C. Chen, Z. Zhang, X.-L. Sheng, S. A. Yang, and G. Su, Phys. Rev. B **100**, 064408 (2019).

[19] P. Jiang, L. Li, Z. Liao, Y. X. Zhao, and Z. Zhong, Nano Lett. **18**, 3844-3849 (2018).

[20] Z. Liu, J. Liu, and J. Zhao, Nano Res. **10**, 1972-1979 (2017).

[21] X. Kong, L. Li, O. Leenaerts, W. Wang, X.-J. Liu, and F. M. Peeters, Nanoscale **10**, 8153-8161 (2018).

[22] L. Li, X. Kong, X. Chen, J. Li, B. Sanyal, and F. M. Peeters, Appl. Phys. Lett. **117**, 143101 (2020).

[23] Z.-Z. Lin, and X. Chen, Appl. Surf. Sci. **529**, 147129 (2020).

[24] G. Kresse, and J. Hafner, Phys. Rev. B **48**, 13115-13118 (1993).

[25] G. Kresse, and J. Furthmüller, Phys. Rev. B **54**, 11169-11186 (1996).

[26] G. Kresse, and D. Joubert, Phys. Rev. B **59**, 1758-1775 (1999).

[27] J. P. Perdew, K. Burke, and M. Ernzerhof, Phys. Rev. Lett. **77**, 3865-3868 (1996).

[28] A. Togo, and I. Tanaka, Scripta Mater. **108**, 1-5 (2015).

[29] X. Qian, J. Liu, L. Fu, and J. Li, Science **346**, 1344-1347 (2014).

[30] X. Li, Z. Zhang, and H. Zhang, Nanoscale Adv. **2**, 495-501 (2020).

[31] K. Sugawara, Y. Nakata, R. Shimizu, P. Han, T. Hitosugi, T. Sato, and T. Takahashi, ACS Nano **10**, 1341-1345 (2016).

[32] K. Zhang, B. Jin, Y. Gao, S. Zhang, H. Shin, H. Zeng, and J. H. Park, Small **15**, 1804903 (2019).

[33] Y. Yu, F. Yang, X. F. Lu, Y. J. Yan, Y.-H. Cho, L. Ma, X. Niu, S. Kim, Y.-W. Son, D. Feng, S. Li, S.-

W. Cheong, X. H. Chen, and Y. Zhang, Nature Nanotech. **10**, 270-276 (2015).

[34] M. Esters, R. G. Hennig, and D. C. Johnson, Phys. Rev. B **96**, 235147 (2017).

[35] M. Bonilla, S. Kolekar, Y. Ma, H. C. Diaz, V. Kalappattil, R. Das, T. Eggers, H. R. Gutierrez, M.-H. Phan, and M. Batzill, Nature Nanotech. **13**, 289-293 (2018).

[36] A. Ghobadi, T. G. U. Ghobadi, A. K. Okyay, and E. Ozbay, Photonics Res. **6**, 244-253 (2018).

[37] Please see Supplemental Material: Phonon spectra (Part I), Spin-polarized electron density and Curie temperature for 1T-$LuN_2$ (Part II), Projected band structures without SOC of 1T-$LuN_2$ (Part III), Chern numbers and Berry curvatures (Part IV), and Weyl-like points (Part V).

[38] S. Lin, W. Li, S. Li, X. Zhang, Z. Chen, Y. Xu, Y. Chen, and Y. Pei, Joule **1**, 816-830 (2017).

[39] X. Chen, D. Wang, X. Liu, L. Li, and B. Sanyal, J. Phys. Chem. Lett. **11**, 2925-2933 (2020).

[40] J. Zhou, and Q. Sun, J. Am. Chem. Soc. **133**, 15113-15119 (2011).

[41] X.-Y. Li, M.-H. Zhang, M.-J. Ren, and C.-W. Zhang, Phys. Chem. Chem. Phys. **22**, 27024-27030 (2020).

[42] J. Sun, X. Zhong, W. Cui, J. Shi, J. Hao, M. Xu, and Y. Li, Phys. Chem. Chem. Phys. **22**, 2429-2436 (2020).

[43] H. L. Zhuang, and R. G. Hennig, Phys. Rev. B **93**, 054429 (2016).

[44] R. C. O'Handley, Modern Magnetic Materials: Principles and Applications, Wiley (New York) chapter 6, page 184 (1999).

[45] H. Chen, P. Tang, and J. Li, Phys. Rev. B **103**, 195402 (2021).

[46] J. M. Kosterlitz, and D. J. Thouless, J. Phys. C: Solid State Phys. **6**, 1181-1203 (1973).

[47] B. Huang, G. Clark, E. Navarro-Moratalla, D. R. Klein, R. Cheng, K. L. Seyler, D. Zhong, E. Schmidgall, M. A. McGuire, D. H. Cobden, W. Yao, D. Xiao, P. Jarillo-Herrero, and X. Xu, Nature **546**, 270-273 (2017).

[48] Y. Deng, Y. Yu, Y. Song, J. Zhang, N. Z. Wang, Z. Sun, Y. Yi, Y. Z. Wu, S. Wu, J. Zhu, J. Wang, X. H. Chen, and Y. Zhang, Nature **563**, 94-99 (2018).

[49] F. Li, B. Yang, Y. Zhu, X. Han, and Y. Yan, Appl. Surf. Sci. **505**, 144648 (2020).

[50] V. K. Gudelli, and G.-Y. Guo, New J. Phys. **21**, 053012 (2019).

[51] X. Lu, R. Fei, L. Zhu, and L. Yang, Nat. Commun. **11**, 4724 (2020).

[52] H. L. Zhuang, P. R. C. Kent, and R. G. Hennig, Phys. Rev. B **93**, 134407 (2016).

[53] S. Skaftouros, K. Ö zdoğan, E. Şaşıoğlu, and I. Galanakis, Appl. Phys. Lett. **102**, 022402 (2013).

[54] R. A. de Groot, F. M. Mueller, P. G. van Engen, and K. H. J. Buschow, Phys. Rev. Lett. **50**, 2024-2027 (1983).

[55] C. Tang, K. Ostrikov, S. Sanvito, and A. Du, Nanoscale Horiz. **6**, 43-48 (2021).

[56] Q. S. Wu, S. N. Zhang, H.-F. Song, M. Troyer, and A. A. Soluyanov, Comput. Phys. Commun. **224**, 405-416 (2018).

[57] A. A. Mostofi, J. R. Yates, Y.-S. Lee, I. Souza, D. Vanderbilt, and N. Marzari, Comput. Phys. Commun. **178**, 685-699 (2008).

[58] A. A. Mostofi, J. R. Yates, G. Pizzi, Y.-S. Lee, I. Souza, D. Vanderbilt, and N. Marzari, Comput. Phys. Commun. **185**, 2309-2310 (2014).

[59] M. P. López Sancho, J. M. López Sancho, and J. Rubio, J. Phys. F: Met. Phys. **15**, 851-858 (1985).

[60] Z. Liu, W. Feng, H. Xin, Y. Gao, P. Liu, Y. Yao, H. Weng, and J. Zhao, Mater. Horiz. **6**, 781-787 (2019).

[61] Z. Liu, L. Li, L. Cui, Y. Shi, T. Song, J. Cai, X. Cui, X. Jiang, and J. Zhao, Nanoscle Horiz. **6**, 283-289 (2021).

[62] H. Weyl, PNAS **15**, 323-334 (1929).

[63] N. P. Armitage, E. J. Mele, and A. Vishwanath, Rev. Mod. Phys. **90**, 015001 (2018).

[64] X. Feng, J. Zhu, W. Wu, and S. A. Yang, arXiv:2103.13772 (2021).

[65] X. Zhou, R.-W. Zhang, Z. Zhang, D.-S. Ma, W. Feng, Y. Mokrousov, and Y. Yao, J. Phys. Chem. Lett. **10**, 3101-3108 (2019).

[66] I. Marković, C. A. Hooley, O. J. Clark, F. Mazzola, M. D. Watson, J. M. Riley, K. Volckaert, K. Underwood, M. S. Dyer, P. A. E. Murgatroyd, K. J. Murphy, P. Le Fèvre, F. Bertran, J. Fujii, I. Vobornik, S. Wu, T. Okuda, J. Alaria, and P. D. C. King, Nat. Commun. **10**, 5485 (2019).

[67] C. Chen, L. Fang, G. Zhao, X. Liu, J. Wang, L. A. Burton, Y. Zhang, and W. Ren, J. Mater. Chem. C **9**, 9539-9544 (2021).

[68] S. Nie, H. Weng, and F. B. Prinz, Phys. Rev. B **99**, 035125 (2019).

[69] D. Gresch, G. Autès, O. V. Yazyev, M. Troyer, D. Vanderbilt, B. Andrei Bernevig, and A. A. Soluyanov, Phys. Rev. B **95**, 075146 (2017).

[70] X. Wang, J. R. Yates, I. Souza, and D. Vanderbilt, Phys. Rev. B **74**, 195118 (2006).

[71] W. Meng, X. Zhang, Y. Liu, L. Wang, X. Dai, and G. Liu, Appl. Surf. Sci. **540**, 148318 (2021).

[72] T. He, X. Zhang, Y. Liu, X. Dai, G. Liu, Z.-M. Yu, and Y. Yao, Phys. Rev. B **102**, 075133 (2020).

[73] S. He, P. Zhou, Y. Yang, W. Wang, and L. Z. Sun, Nanoscale Adv. **3**, 3093-3099 (2021).

[74] W.-X. Ji, B.-M. Zhang, S.-F. Zhang, C.-W. Zhang, M. Ding, P.-J. Wang, and R. Zhang, Nanoscale **10** 13645-13651 (2018).

[75] L. Jin, L. Wang, X. Zhang, Y. Liu, X. Dai, H. Gao, and G. Liu, Nanoscale **13**, 5901-5909 (2021).

[76] W. Fan, S. Nie, C. Wang, B. Fu, C. Yi, S. Gao, Z. Rao, D. Yan, J. Ma, M. Shi, Y. Huang, Y. Shi, Z. Wang, T. Qian, and H. Ding, Nat. Commun. **12**, 2052 (2021).

[77] Z. Liu, G. Zhao, B. Liu, Z. F. Wang, J. Yang, and F. Liu, Phys. Rev. Lett. **121**, 246401 (2018).

[78] X. Liu, H.-C. Hsu, and C.-X. Liu, Phys. Rev. Lett. **111**, 086802 (2013).

[79] Y. Ren, J. Zeng, X. Deng, F. Yang, H. Pan, and Z. Qiao, Phys. Rev. B **94**, 085411 (2016).

[80] P. Zhong, Y. Ren, Y. Han, L. Zhang, and Z. Qiao, Phys. Rev. B **96**, 241103(R) (2017).

[81] F. Zhou, Y. Liu, M. Kuang, P. Wang, J. Wang, T. Yang, X. Wang, Z. Cheng, and G. Zhang, Nanoscale **13**, 8235-8241 (2021).

[82] Y. Shi, L. Li, X. Cui, T. Song, and Z. Liu, Phys. Status Solidi-R. **15**, 2100115 (2021).

[83] Y. Hu, S.-S. Li, W.-X. Ji, C.-W. Zhang, M. Ding, P.-J. Wang, and S.-S. Yan, J. Phys. Chem. Lett. **11** 485-491 (2020).

[84] Y.-F. Zhao, R. Zhang, R. Mei, L.-J. Zhou, H. Yi, Y.-Q. Zhang, J. Yu, R. Xiao, K. Wang, N. Samarth, M. H. W. Chan, C.-X. Liu, and C.-Z. Chang, Nature **588**, 419-423 (2020).

[85] X. Kong, L. Li, L. Liang, F. M. Peeters, and X.-J. Liu, Appl. Phys. Lett. **116**,192404 (2020).